*Progress In Electromagnetics Research M, Vol. 64, 181–192, 2018*

# Efficacy of Magnetic and Capacitive Hyperthermia on Hepatocellular Carcinoma

**Chien-Chang Chen and Jean-Fu Kiang***

**Abstract**—The efficacy of applying magnetic hyperthermia (MHT) and capacitive hyperthermia (CHT) to treat hepatocellular carcinoma (HCC) is studied. Magnetoquasistatic (MQS) and electroquasistatic (EQS) formulations are developed to compute the magnetic field and electric field distributions, respectively, which are numerically solved by using finite element method. The heat transport equation is applied to compute the temperature distribution in the treated area. Simulation results of temperature distribution are used to compare the efficacy of MHT and CHT.

## 1. INTRODUCTION

Hepatocellular carcinoma (HCC) is a primary malignancy in human livers [1]. Patients carrying advanced HCC without treatment were reported to have a mean survival time of less than four months [1]. Most of them cannot be cured [1, 2], but a few patients can be treated by surgical resection and transplantation. Typical treatments on HCC include intratumoral injection of absolute ethanol or acetic acid, invasive thermal destruction by using microwave or radio-frequency (RF) needles [3], transarterial chemoembolization (TACE) with drug-elutriating beads [1, 4], and so on. Among these approaches, regional therapies tend to increase the median survival time, although not significantly [1].

Hyperthermia (HT) treatment [5] is conducted by delivering RF power to a malignant tumor and raises its temperature up to 42–45°C [6] over a period of 50 minutes [7]. Compared with radiotherapy and chemotherapy, HT induced less side effects [2]. Different types of HT techniques have been proposed, including capacitive [8], magnetic (inductive) [5, 9], antenna array [10], ultrasound [11] and interstitial [12].

To practice magnetic hyperthermia (MHT), small magnetic particles with diameter less than 100 nm were injected to a tumor before it was heated with an alternating magnetic field [2]. Such MHT plan has the advantage of controllable heat source [13], and two major issues need to be considered, the maximum tolerable magnitude of magnetic field and the choice of magnetic nanoparticles [1, 4]. Rats with HCC were treated with the combination of chemotherapy and MHT, in which case nanoparticles were made of carbon-coated iron [14] or $\gamma$-$Fe_2O_3$ [15].

Capacitive hyperthermia (CHT) is another type of HT, which relies on the electric field to deliver heat [8]. Gold nanoparticles can be injected to focus the heating area [1]. CHT has been used for treating HCC, as an adjunctive method to radiotherapy [16], chemotherapy [7] and immunotherapy [17].

In this work, both MHT and CHT plans are analyzed, starting from their working principles. Finite element method is then applied to simulate the field distribution in the treated area, and heat transport equation is solved to obtain the temperature distribution, which is used to compare the efficacy of different methods in treating HCC. The rest of this paper is organized as follows: The theory of MHT and bio-heat equation are presented in Section 2 and Section 3, respectively, MHT treatment on HCC is simulated in Section 4, the theory of CHT and its simulation results are presented in Section 5 and Section 6, respectively. Finally, some conclusions are drawn in Section 7.

*Received 19 October 2017, Accepted 31 January 2018, Scheduled 10 February 2018*

* Corresponding author: Jean-Fu Kiang (jfkiang@ntu.edu.tw).

The authors are with the Graduate Institute of Communication Engineering, National Taiwan University, Taipei 106, Taiwan, R. O. C.

## 2. THEORY OF MAGNETIC HYPERTHERMIA

The magnetic vector potential can be decomposed into components of different orders as $\bar{A}(\bar{r}) = \bar{A}^{(0)}(\bar{r}) + \bar{A}^{(1)}(\bar{r}) + \bar{A}^{(2)}(\bar{r}) + \cdots$ [18]. When the operation frequency is sufficiently low, the magnetic field can be approximated as a static one, characterized with the zeroth-order magnetic vetcor potential $\bar{A}^{(0)}(\bar{r})$ that satisfies

$$\nabla \times \frac{1}{\mu(\bar{r})} \nabla \times \bar{A}^{(0)}(\bar{r}) = \bar{J}(\bar{r}) \tag{1}$$

where $\bar{J}(\bar{r})$ is the volume current density (A/m$^2$) in the abdominal model. To solve Eq. (1) with finite element method, the computational domain is first divided into a set of adjoining tetrahedra, and $\bar{A}^{(0)}(\bar{r})$ is expanded in terms of the Whitney-1 form elements $\bar{\omega}_n(\bar{r})$'s defined in these tetrahedra as [19, 20]

$$\bar{A}^{(0)}(\bar{r}) = \sum_{n=1}^{N_e} a_n^{(0)} \bar{\omega}_n(\bar{r}) \tag{2}$$

where $N_e$ is the total number of edges, and $\bar{\omega}_n(\bar{r})$ has unit tangential component over the $n$th edge which lies in one of these tetrahedra. By substituting Eq. (2) into Eq. (1), then applying the Petrov-Galerkin procedure [20], a matrix equation is derived as

$$\bar{\bar{K}}_1 \cdot \bar{a}^{(0)} = \bar{b}_k^{(0)} \tag{3}$$

where $\bar{\bar{K}}_1$ is a coefficient matrix; $\bar{a}^{(0)}$ contains the tangential magnetic vector potentials on all the edges; $\bar{b}_k^{(0)}$ is derived from the volume current density $\bar{J}(\bar{r})$ and possible surface current density. A generalized minimal residual (GMRES) method [21] is then applied to solve Eq. (3) for $\bar{a}^{(0)}$.

Once $\bar{A}^{(0)}$ is obtained, the electric field can be computed as

$$\bar{E}^{(1)}(\bar{r}) = -j\omega \bar{A}^{(0)} = -j\omega \sum_{n=1}^{6} a_n^{(0)} \bar{\omega}_n(\bar{r}) \tag{4}$$

which is a first-order quantity in terms of $\omega$. The relaxation heat loss (watt/m$^3$) of magnetic field, attributed to magnetic nanoparticles, is computed as [22]

$$Q_{\mathrm{em}}(\bar{r}) \simeq \frac{\omega \mu_0 \mu''(\bar{r})}{2} \left| \bar{H}^{(0)}(\bar{r}) \right|^2 \tag{5}$$

where $\mu_0 \mu''(\bar{r})$ is the imaginary part of permeability.

## 3. BIO-HEAT EQUATION

The temperature distribution in the abdominal model satisfies the bio-heat equation [23]

$$\rho(\bar{r}) c(\bar{r}) \frac{\partial T(\bar{r}, t)}{\partial t} = \nabla \cdot [\zeta(\bar{r}) \nabla T(\bar{r}, t)] - \xi(\bar{r}) \rho(\bar{r}) \rho_b c_b [T(\bar{r}, t) - T_b] + Q_s(\bar{r}, t) \tag{6}$$

where $\rho(\bar{r})$ and $c(\bar{r})$ (J/kg/K) are the mass density (kg/m$^3$) and heat capacity (J/kg/K), respectively, of the tissues; $\rho_b$ and $c_b$ are the mass density and heat capacity, respectively, of the blood; $\zeta(\bar{r})$ (watt/m/K) and $T(\bar{r}, t)$ (K) are the thermal conductivity and temperature, respectively, of the tissues; $\xi(\bar{r})$ (m$^3$/kg/s) is the blood flow rate per-unit-mass in the tissues; $T_b$ is the temperature of the blood, which is approximated as a constant; and $Q_s(\bar{r}, t)$ (watt/m$^3$) is the heat source, which is decomposed as

$$Q_s(\bar{r}, t) = Q_{\mathrm{met}}(\bar{r}, t) + Q_{\mathrm{em}}(\bar{r}, t)$$

where $Q_{\mathrm{met}}(\bar{r}, t)$ (watt/m$^3$) is the metabolic heat generation.

The temperature distribution can be expanded in terms of the Whitney-0 form elements $\lambda_n(\bar{r})$'s defined in the same set of tetrahedra as [19, 20]

$$T(\bar{r}, t) = \sum_{n=1}^{N_v} b_n(t) \lambda_n(\bar{r}) \tag{7}$$

where $N_v$ is the total number of vertex points. By substituting Eq. (7) into Eq. (6), then applying the Crank-Nicholson finite difference scheme [24] and Petrov-Galerkin procedure [20], a matrix equation is derived as

$$\left(\bar{\bar{U}} + \bar{\bar{V}}\right) \cdot \bar{b}(t + \Delta t) = \left(\bar{\bar{U}} - \bar{\bar{V}}\right) \cdot \bar{b}(t) + \bar{d}(t) \tag{8}$$

where $\bar{\bar{U}}$ and $\bar{\bar{V}}$ are coefficient matrices; $\bar{b}(t)$ contains the temperature at all the vertices; $\bar{d}(t)$ is derived from $T_b$ and $Q_s(\bar{r}, t)$. The GMRES method [21] is then applied to solve Eq. (8) for $\bar{b}(t)$, which characterizes the time evolution of temperature distribution in the treated region.

## 4. MAGNETIC HYPERTHERMIA PLAN

Figure 1 shows an abdominal model including HCC, where the torso is surrounded by a bolus and a thin current sheet. Patients with cirrhosis have a high risk of developing HCC [3], hence the spherical HCC is surrounded by cirrhotic parenchyma in the model. Fig. 1(c) shows a canonical semi-ellipsoid liver model in the $xyz$ coordinates, which is rotated about the $z$ axis by $\phi$, then about the $y$ axis by $\theta$ and finally about the $x$ axis by $\psi$, to be properly oriented inside the abdomen.

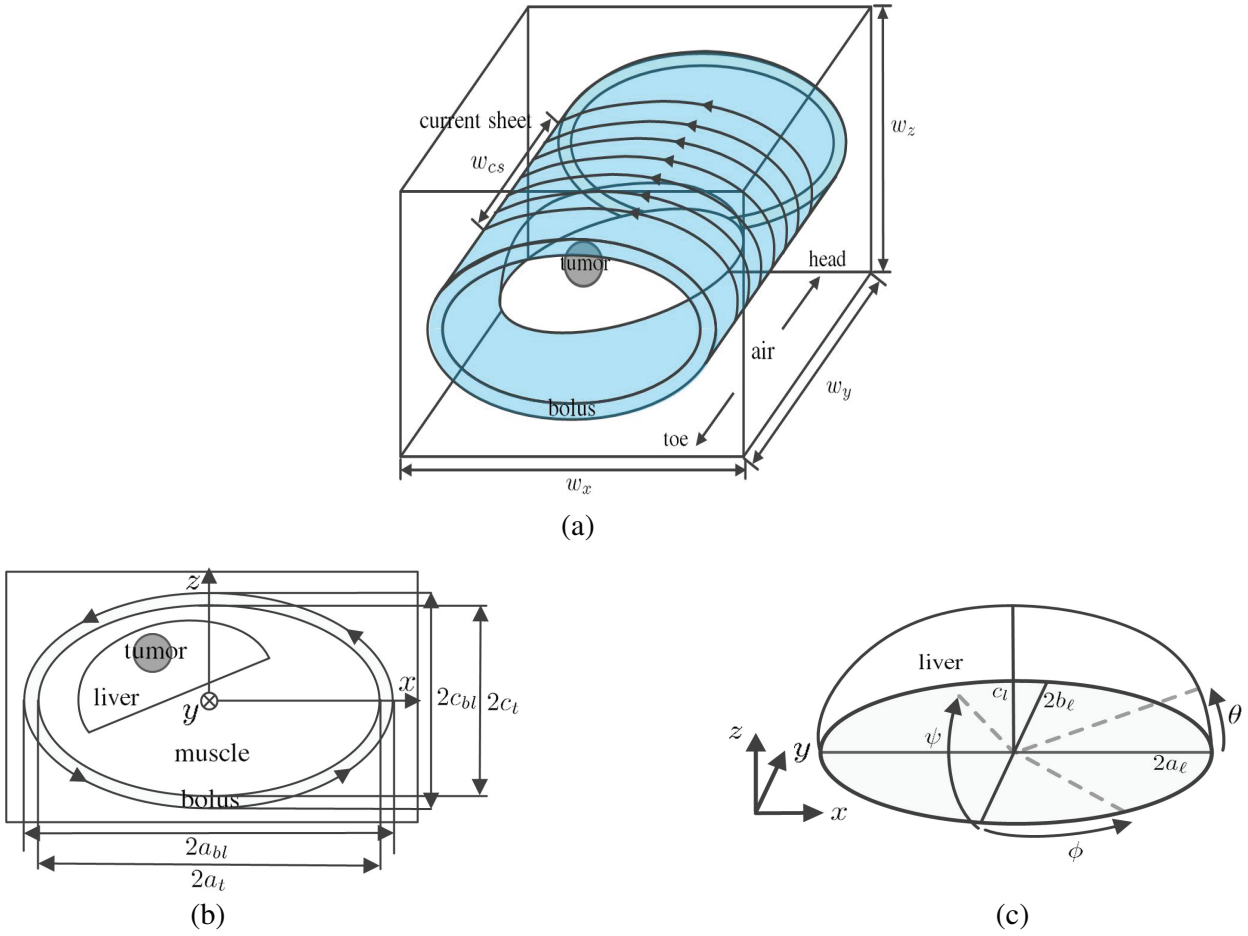


**Figure 1.** Abdominal model in MHT plan, (a) panoramic view, (b) cross-sectional view and (c) liver model. The grey sphere marks an HCC.

Table 1 lists the geometrical parameters of the abdominal model in the simulations. The size of the computational domain is $(w_x, w_y, w_z)$. The semi-axes of the ellipsoid are labeled as $a$, $b$ and $c$ in $x$, $y$ and $z$ directions, respectively; subscripts $\ell$, $t$ and $bl$ stand for liver, torso and bolus, respectively. The width of current sheet in the $y$ direction is $w_{cs}$.

**Table 1.** Geometrical parameters (in unit of cm) of abdominal model in MHT.

| | size | center |
|---|---|---|
| computational domain | $(w_x, w_y, w_z) = (50, 26, 40)$ | - |
| torso | $(2a_t, w_y, 2c_t) = (30, 26, 22)$ | - |
| bolus | $(2a_{bl}, w_y, 2c_{bl}) = (34, 26, 26)$ | - |
| cirrhotic liver | $(2a_\ell, 2b_\ell, 2c_\ell) = (20, 16, 14)$<br>$\theta = \pi/8$, $\phi = \pi/4$<br>$\psi = 3\pi/8$ | $(-3, 0, 1)$ |
| tumor | $2r = 4$ | $(-6, 1, 5)$ |
| current sheet | $(2a_{bl}, w_{cs}, 2c_{bl}) = (34, 12, 26)$ | $(0, 0, 0)$ |

Table 2 lists the electric properties of the abdominal model and the bolus. In pure water, the imaginary part of complex dielectric constant is 13.90 [27], equivalent to $\sigma = 0.000927$, which is approximated as zero in the simulations.

**Table 2.** Electrical properties of abdominal model.

| | MHT, 1.2 MHz | CHT, 8 MHz | |
|---|---|---|---|
| | $\sigma$ (S/m) | $\epsilon_r$ | $\sigma$ (S/m) |
| bolus | $\simeq 0$ | 172 [23] | 0.69 [23] |
| muscle | 0.54 [25] | 172 [25] | 0.69 [25] |
| cirrhotic liver | 0.324 [26] | 338 [26] | 0.42 [26] |
| HCC | 0.324 [26] | 338 [26] | 0.42 [26] |

Table 3 lists the thermal parameters of liver tissues. The mass densities of cirrhotic liver, liver tumor and blood are 1,040 [28], 1,100 [29] and 1,000 (kg/m$^3$) [30], respectively. The blood perfusion rate $\xi$ in the HCC is higher than that in its surrounding cirrhotic parenchyma [31–33]. Their values are 3.3 and 1 (kg/m$^3$/s) [31], respectively; or $3.17 \times 10^{-6}$ and $0.91 \times 10^{-6}$ (m$^3$/kg/s, respectively. Typical metabolic rate of human liver is 200 (kcal/kg/day) [34] or 9,689 (watt/m$^3$), assuming the mass density of liver is 1,100 (kg/m$^3$) [29]. The metabolic rate of liver tumor is 6.807 (watt/kg) [35] or 7,079.28 (watt/m$^3$), assuming the mass density of tumor is 1,040 (kg/m$^3$) [28]. The values of $\zeta$, $c$ and $Q_{\rm met}$ of cirrhotic liver are approximated as those of normal liver. The value of $\xi$ in a cirrhotic liver could be 2 (kg/m$^3$/s) [36] or $1.82 \times 10^{-6}$ (m$^3$/kg/s), assuming the mass densities of cirrhotic liver and blood are 1,100 [29] and 1,000 (kg/m$^3$) [30], respectively. The value of $\xi$ in an HCC could be 46.3 (ml/100 g/min) or $7.72 \times 10^{-6}$ (m$^3$/kg/s) [33].

**Table 3.** Thermal parameters of liver tissues.

| | $\zeta$ (W/m/K) | $\rho$ (kg/m$^3$) | $c$ (J/kg/K) | $\xi$ (m$^3$/kg/s) | $Q_{\rm met}$ (W/m$^3$) |
|---|---|---|---|---|---|
| muscle | 0.6 [23] | 1,020 [23] | 3,500 [23] | $\xi_{\rm muscle}$ [37] | 4,200 [8] |
| cirrhotic liver parenchyma | 0.48 [38] | 1,100 [29] | 3,600 [38] | $0.91 \times 10^{-6}$ [28, 30, 31] | 9,689 [29, 34] |
| HCC | 0.57 [28] | 1,040 [28] | 3,960 [28] | $3.17 \times 10^{-6}$ [29–31] | 7,079 [28, 35] |
| blood | - | 1,000 [30] | 4,180 [30] | - | - |

The temperature-dependent blood perfusion rate of human muscle (in $m^3/kg/s$) can be modeled as [37]

$$\xi_{\text{muscle}} = \begin{cases} 4.41 \times 10^{-7} + 3.48 \times 10^{-6} e^{-(T-45)^2/12}, & T \leq 45 \\ 3.92 \times 10^{-6}, & T > 45 \end{cases} \tag{9}$$

where $T$ is the temperature (in °C). It was reported that the perfusion rate in human tumors can be approximated as a constant during the whole process of hyperthermia treatment, with temperature up to 44° [39]. The simulated temperature distributions with temperature-dependent perfusion rate is similar to that with constant perfusion rate. It is observed that the volume of peripheral muscle affected by the low-temperature bolus is broader with temperature-dependent $\xi$ than that with constant $\xi$, because less warm blood is supplied to muscle as temperature falls below 36°C in the former case.

The central area of muscle is raised to a higher temperature with temperature-dependent $\xi$, as compared to that with constant $\xi$. The temperature distribution is determined by the deposition of electromagnetic and metabolic energies, as well as the blood perfusion rate and the thermal conductivity of the tissues. Balanced temperature distribution is reached when the heat deposition is equal to the heat removal by blood perfusion and thermal conduction. Larger volume of peripheral muscle at lower temperature enhances heat conduction, leading to higher temperature in the muscle. It is also observed that the liver parenchyma has larger overheated volume with temperature-dependent $\xi$ than that with constant $\xi$, possibly caused by inward heat conduction from the muscle.

The product of magnetic field and frequency is restricted to about $5 \times 10^8$ (A/m/s) in applying HT to the thorax region [40]. If the same restriction is imposed, at $f = 1.2\,\text{MHz}$, the maximum magnetic

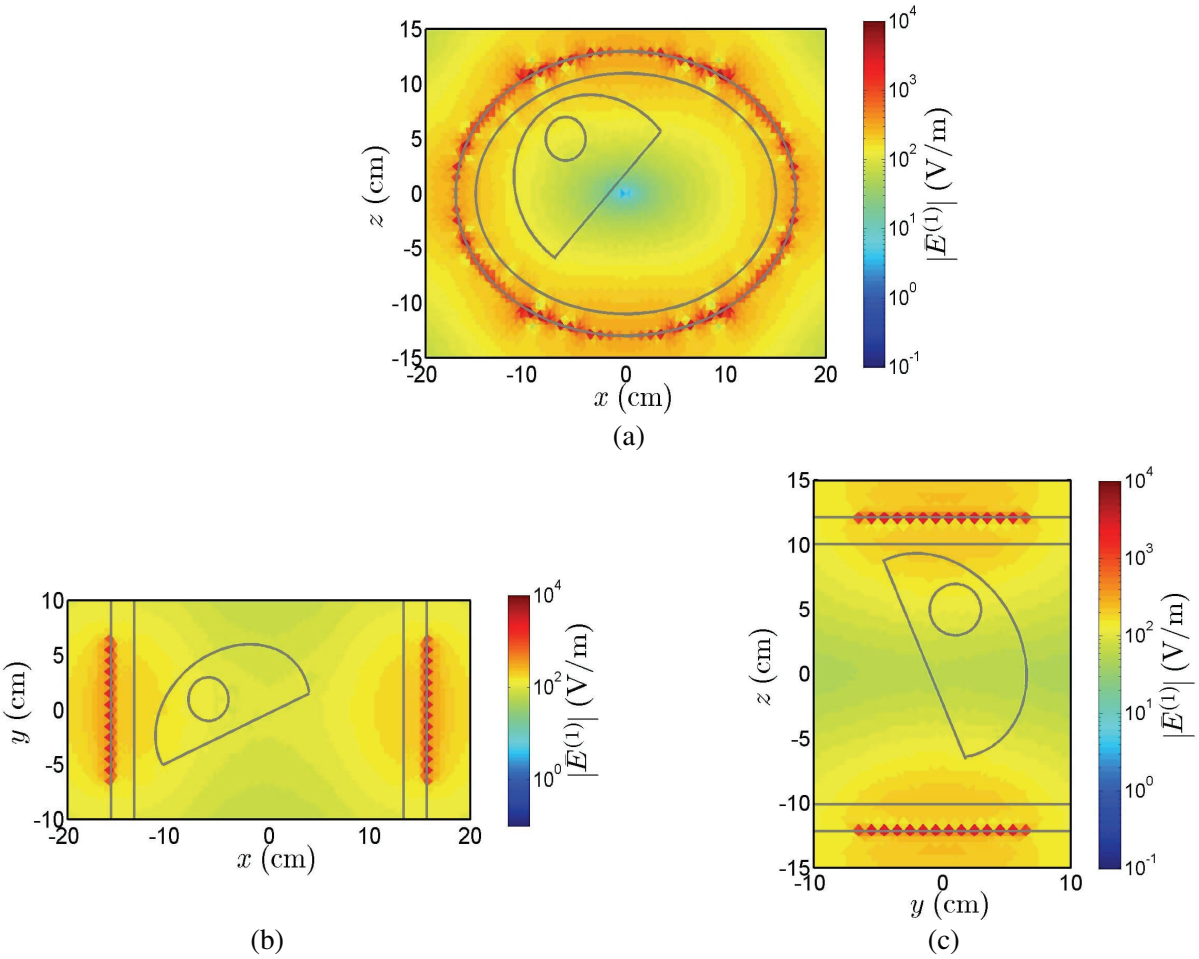


**Figure 2.** Magnitude of $\bar{E}^{(1)}(\bar{r})$ in (a) $xz$ plane, (b) $xy$ plane and (c) $yz$ plane.

field would be about 400 (A/m). If the tumor density is $\rho = 1,040\,(\mathrm{kg/m^3})$ [28], a desirable SAR of 50 (watt/kg) [40] leads to $Q_{\mathrm{rel}} \simeq 5.2 \times 10^4$ (watt/m$^3$), and the magnetic field inside the tumor is about 175 (A/m). The imaginary part of complex permeability is a function of both the magnetic field strength and the frequency. Take $Fe_3O_4$ in solution for example, $\mu'' = 058$ at $f = 150\,\mathrm{kHz}$ and

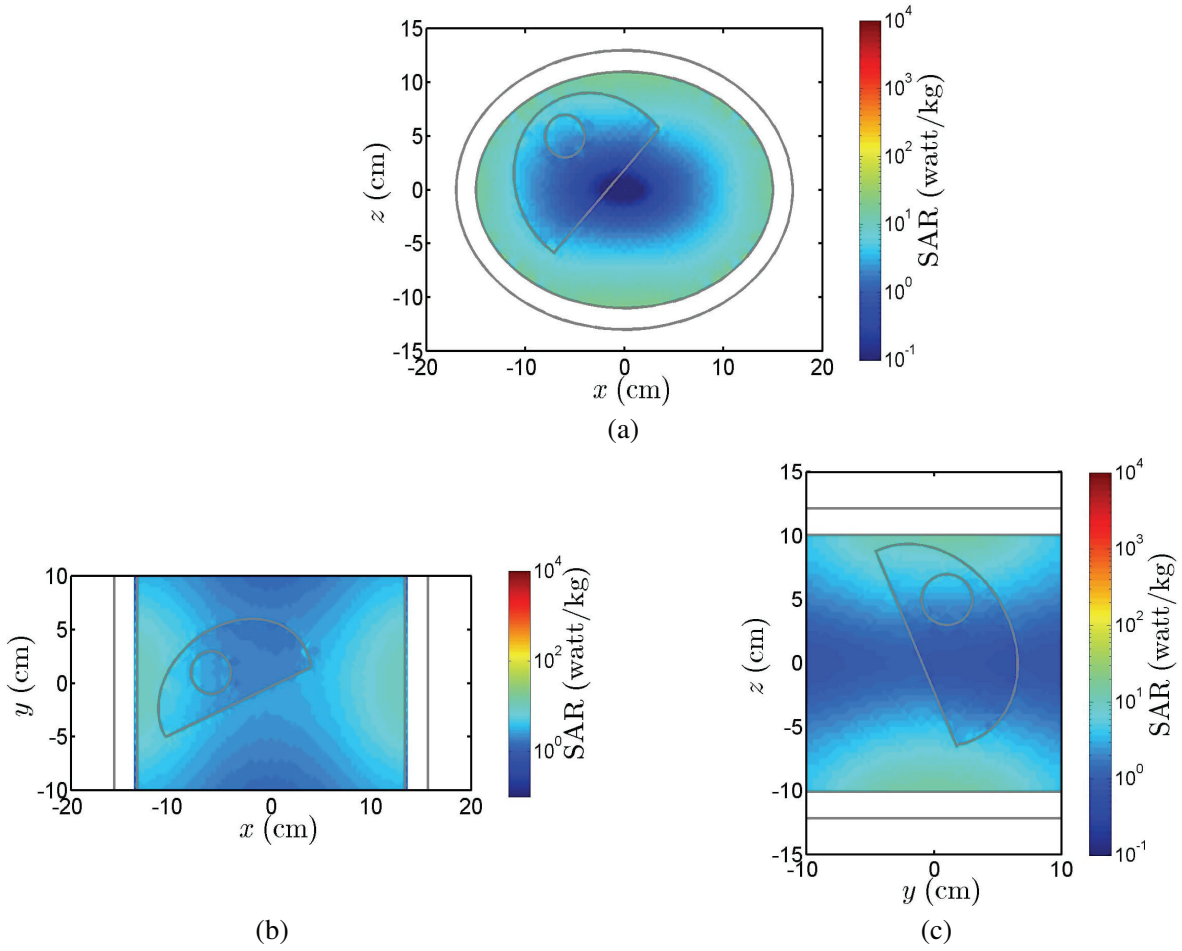


**Figure 3.** SAR distribution in (a) $xz$ plane, (b) $xy$ plane and (c) $yz$ plane.

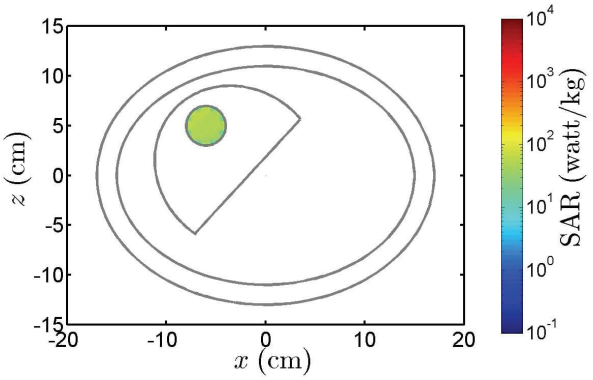


**Figure 4.** SAR distribution attributed to magnetic nanoparticles.

$|\bar{H}| = 400\,\mathrm{A/m}$ [41]. In the simulations, $\mu''(\bar{r})$ in the tumor is estimated by using (5) as

$$\mu''(\bar{r}) = \frac{2Q_{\mathrm{rel}}(\bar{r})}{\omega\mu_0 \left|\bar{H}(\bar{r})\right|^2} = \frac{2 \times 5.2 \times 10^4}{2 \times \pi \times 1.2 \times 10^6 \times \mu_0 \times 175^2} \simeq 0.3584$$

Figure 2 shows the magnitude of the first-order electric field, $\bar{E}^{(1)}(\bar{r})$. It is observed that the electric field is stronger near the current sheet, and the polarization of $\bar{E}^{(1)}(\bar{r})$ is the same as that of $\bar{A}^{(0)}$. Fig. 3 shows the SAR distribution in the tissues, which ranges from 1 to 8 (watt/kg) in the tumor. Fig. 4 shows the SAR distribution attributed to magnetic nanoparticles. The magnitude of SAR is higher in the peripheral area (58 watt/kg) than in the central area (50 watt/kg). The imaginary part of permeability outside the tumor is approximated as zero, hence no electromagnetic energy is deposited there. Fig. 5 shows the temperature distribution in the abdominal model under MHT for 50 minutes. The temperature in the tumor is raised up to 40.86°C, which is higher than its surrounding tissues. No undesirable hot spots are observed.

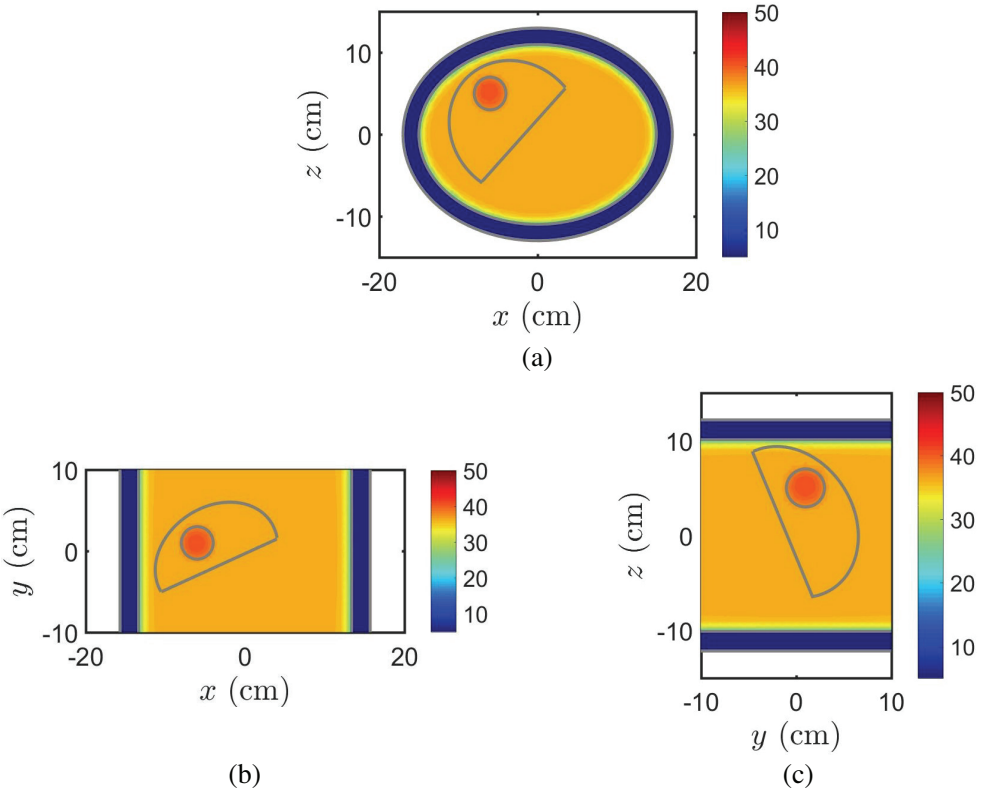


**Figure 5.** Temperature distribution in abdominal model under MHT for 50 minutes, (a) $xz$ plane, (b) $xy$ plane and (c) $yz$ plane.

## 5. THEORY OF CAPACITIVE HYPERTHERMIA

Figure 6 shows the abdominal model in the CHT plan. The electric scalar potential can be decomposed into components of different orders as $\Phi(\bar{r}) = \Phi^{(0)}(\bar{r}) + \Phi^{(1)}(\bar{r}) + \Phi^{(2)}(\bar{r}) + \cdots$ [18]. When the operation frequency is sufficiently low, the electric field can be approximated as a static one, with the zeroth-order electric potential $\Phi^{(0)}(\bar{r})$ satisfying

$$\nabla \cdot \left[\epsilon(\bar{r})\nabla\Phi^{(0)}(\bar{r})\right] = -\rho^{(0)}(\bar{r}) \tag{10}$$

where $\epsilon(\bar{r})$ is the complex permittivity (F/m) of the medium, and $\rho^{(0)}(\bar{r})$ (C/m$^3$) is the zeroth-order charge density in the abdomen. To solve (10), the abdominal region is decomposed into a finite set

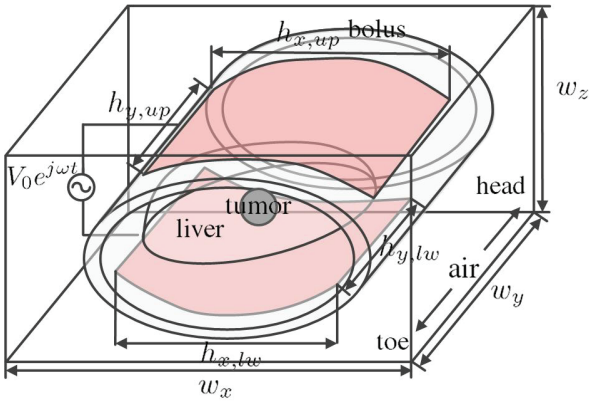


**Figure 6.** Abdominal model in CHT plan.

of adjoining tetrahedra, and the potential distribution $\Phi^{(0)}(\bar{r})$ is expanded in terms of Whitney-0 form elements $\lambda_n(\bar{r})$'s as [19, 20]

$$\Phi^{(0)}(\bar{r}) = \sum_{n=1}^{N_v} \phi_n^{(0)} \lambda_n(\bar{r}) \tag{11}$$

where $N_v$ is the total number of vertex points. By substituting Eq. (11) into Eq. (10) and applying the Petrov-Galerkin procedure [20], we obtain a matrix equation

$$\bar{\bar{S}} \cdot \bar{\phi}^{(0)} = \bar{b}_s \tag{12}$$

where $\bar{\bar{S}}$ is a coefficient matrix; $\bar{\phi}^{(0)}$ contains the zeroth-order electrical potentials at all the vertex points; $\bar{b}_s$ is derived from the potential imposed on the electrodes. A preconditioned GMRES method is then applied to solve Eq. (12) for $\bar{\phi}^{(0)}$ [21].

The arrangement of electrodes as shown in Fig. 6 makes the zeroth-order current $\bar{J}^{(0)}(\bar{r})$ negligible, which implies $\bar{A}^{(0)}(\bar{r}) = 0$ and $\bar{H}^{(0)}(\bar{r}) = 0$, where the zeroth-order magnetic vector potential satisfies $\nabla \times \frac{1}{\mu(\bar{r})} \nabla \times \bar{A}^{(0)}(\bar{r}) = \bar{J}^{(0)}(\bar{r})$. Hence, the electric field can be represented in terms of $\Phi^{(0)}(\bar{r})$ as

$$\bar{E}^{(0)}(\bar{r}) = -\nabla \Phi^{(0)}(\bar{r}) \tag{13}$$

and the power density per unit volume can be represented as [42]

$$Q_{\text{em}}(\bar{r}) = \frac{\sigma(\bar{r})}{2} \left| \bar{E}^{(0)}(\bar{r}) \right|^2 \tag{14}$$

## 6. CAPACITIVE HYPERTHERMIA PLAN

Table 4 lists the geometrical parameters of an abdominal model in the simulations of CHT. A pair of disk electrodes of diameter 25 or 30 cm used in clinic practice [7, 16] are modeled as two conformal rectangular electrodes of size 22 cm × 22 cm. The width $w_y$ is increased to 36 cm such that the electric field becomes negligible near the boundary of the computational domain.

Figure 7 shows the temperature distribution in an HCC patient after a CHT treatment plan, lasting for 50 minutes [7, 16]. The power level is 800 watt [7], which is delivered by setting $V_0 = 90.73$ (V). In clinic practice, the temperature of bolus was maintained at 5°C [7], and an average tumor temperature of 40.3°C could be reached [17]. The simulated tumor temperature is 39.7°C, but unwanted hot spots at about 47°C appear in liver parenchyma. Because the dielectric properties of HCC and its surrounding parenchyma are similar, applying CHT may create collateral burning to tissues near the HCC. Moreover, more blood vessels exist in an HCC than in normal tissues due to hyperplasia, heat convection by blood makes it more difficult to raise the temperature in the HCC without burning the surrounding parenchyma. Hence, cautious measure is required to treat HCC with CHT. In comparison, the heat deposition in MHT plan is focused within the tumor by injecting magnetic nanoparticles to it, thus reducing collateral damage to the surrounding tissues.

**Table 4.** Geometrical parameters (in unit of cm) of abdominal model in CHT.

| | size | position |
|---|---|---|
| computational domain | $(w_x, w_y, w_z) = (50, 36, 40)$ | - |
| torso | $(2a_t, w_y, 2c_t) = (30, 36, 22)$ | - |
| bolus | $(2a_{bl}, w_y, 2c_{bl}) = (34, 36, 26)$ | - |
| cirrhotic liver | $(2a_\ell, 2b_\ell, 2c_\ell) = (20, 16, 14)$<br>$\theta = \pi/8$, $\phi = \pi/4$<br>$\psi = 3\pi/8$ | $(-3, 0, 1)$ |
| tumor | $2r = 4$ | $(-6, 1, 5)$ |
| upper electrode [7] | $(h_{x,up}, h_{y,up}) = (22, 22)$ | $(0, 1, 13)$ |
| lower electrode [7] | $(h_{x,lw}, h_{y,lw}) = (22, 22)$ | $(0, 1, -13)$ |

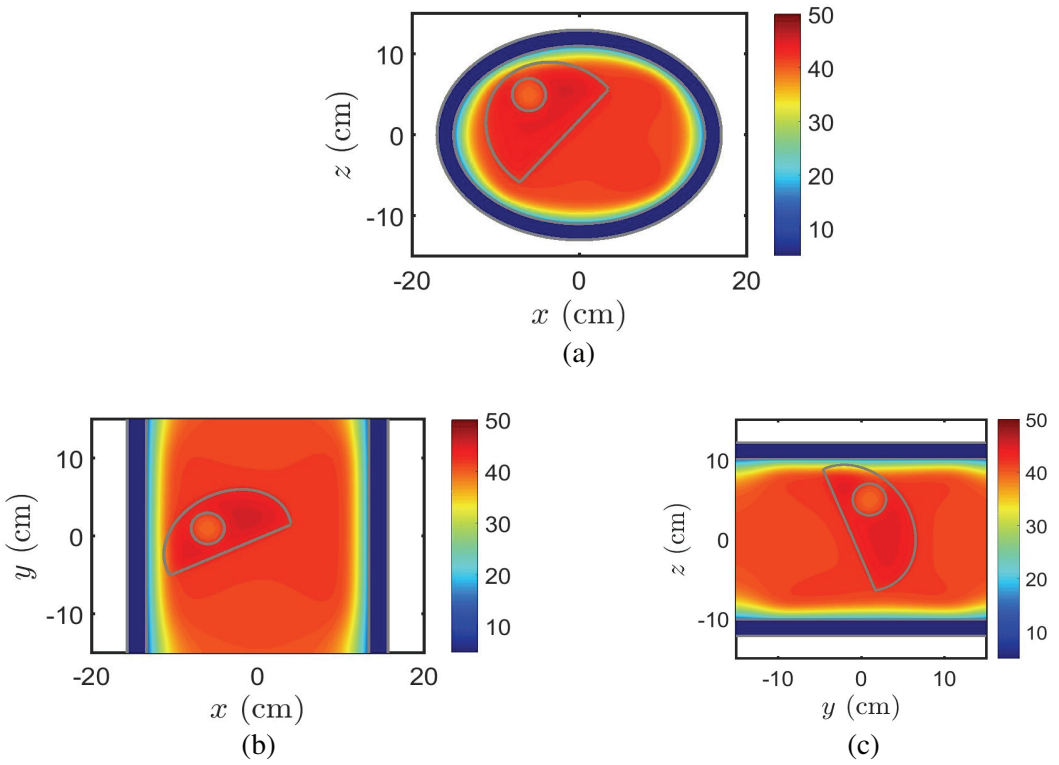


**Figure 7.** Temperature distribution in an HCC patient treated with CHT, $t = 50$ minutes, power level is 800 watt, (a) $xz$ plane, (b) $xy$ plane and (c) $yz$ plane.

## 7. CONCLUSION

The efficacy of MHT and CHT on treating HCC has been analyzed and compared by simulations. Finite element method is used to compute the field distribution in an HCC and its surrounding tissues. The temperature distribution is then computed by solving the heat transport equation. The simulation results show that unwanted temperature rise occurs in cirrhotic liver parenchyma when CHT is applied, while heat deposition is concentrated to HCC when MHT is applied. The proposed method can provide important information to customize a hyperthermia treatment plan in clinic practice.

## ACKNOWLEDGMENT

This work is partly sponsored by the Ministry of Science and Technology, Taiwan, R.O.C., under contract MOST 105-2221-E-002-035 and partly supported by the donation from Pixart Imaging Inc. for promoting science and technology.

## REFERENCES

1. Raoof, M. and S. A. Curley, "Non-invasive radiofrequency-induced targeted hyperthermia for the treatment of hepatocellular carcinoma," *Int. J. Hepatol.*, 676957, May 2011.
2. Moroz, P., S. K. Jones and B. N. Gray, "Status of hyperthermia in the treatment of advanced liver cancer," *J. Surg. Oncol.*, Vol. 77, 259–269, 2001.
3. Crocetti, L. and R. Lencioni, "Thermal ablation of hepatocellular carcinoma," *Cancer Imaging*, Vol. 8, 19–26, 2008.
4. Corr, S. J., B. T. Cisneros, L. Green, M. Raoof, and S. A. Curley, "Protocols for assessing radiofrequency interactions with gold nanoparticles and biological systems for non-invasive hyperthermia cancer therapy," *J. Vis. Exp.*, Vol. 78, e50480, Aug. 2013.
5. Kotsuka, Y., H. Kayahara, K. Murano, H. Matsui, and M. Hamuro, "Local inductive heating method using novel high-temperature implant for thermal treatment of luminal organs," *IEEE Trans. Microwave Theory Tech.*, Vol. 57, No. 10, 2574–2580, Oct. 2009.
6. Iero, D. A. M., T. Isernia, A. F. Morabito, I. Catapano, and L. Crocco, "Optimal constrained field focusing for hyperthermia cancer therapy: A feasibility assessment on realistic phantoms," *Progress In Electromagnetics Research*, Vol. 102, 125–141, 2010.
7. Yamamoto, K. and Y. Anaka, "Radio frequency capacitive hyperthermia for unresectable hepatic cancers," *J. Gastroenterol.*, Vol. 32, 361–366, 1997.
8. Jamil, M. and E. Y. K. Ng, "To optimize the efficacy of bioheat transfer in capacitive hyperthermia: A physical perspective," *J. Therm. Biol.*, Vol. 38, No. 5, 272–279, Jul. 2013.
9. Trujillo-Romero, C. J., S. Garcia-Jimeno, A. Vera-Hernandez, L. Leija-Salas, and J. Estelrich, "Using nanoparticles for enhancing the focusing heating effect of an external waveguide applicator for oncology hyperthermia: Evaluation in muscle and tumor phantoms," *Progress In Electromagnetics Research*, Vol. 121, 343–363, 2011.
10. Vrba, D., D. B. Rodrigues, J. Vrba (Jr.), and P. R. Stauffer, "Metamaterial antenna arrays for improved uniformity of microwave hyperthermia treatments," *Progress In Electromagnetics Research*, Vol. 156, 1–12, 2016.
11. Staruch, R., R. Chopra, and K. Hynynen, "Hyperthermia in bone generated with MR imaging controlled focused ultrasound: Control strategies and drug delivery," *Radiology*, Vol. 263, No. 1, 117–127, Apr. 2012.
12. Chen, X., C. J. Diederich, J. H. Wootton, J. Pouliot, and I-C. Hsu, "Optimisation-based thermal treatment planning for catheter-based ultrasound hyperthermia," *Int. J. Hyperthermia*, Vol. 26, No. 1, 39–55, Feb. 2010.
13. Jordan, A., P. Wust, H. Fähling, W. John, A. Hinz, and R. Felix, "Inductive heating of ferrimagnetic particles and magnetic fluids: Physical evaluation of their potential for hyperthermia," *Int. J. Hyperthermia*, Vol. 9, No. 1, 51–68, Jan.–Feb. 1993.
14. Li, F.-E., W.-H. Yan, Y.-H. Guo, H. Qi, and H.-X. Zhou, "Preparation of carboplatin-Fe@C-loaded chitosan nanoparticles and study on hyperthermia combined with pharmacotherapy for liver cancer," *Int. J. Hyperthermia*, Vol. 25, No. 5, 383–391, Aug. 2009.
15. Chang, P. E. J., S. Purushotham, H. Rumpel, I. H. C. Kee, R. T. H. Ng, P. K. H. Chow, R. V. Ramanujan, and C. K. Tan, "Novel dual magnetic drug targeting and hyperthermia therapy in hepatocellular carcinoma with thermosensitive polymer-coated nanoparticles," *J. Gastroint. Dig. Syst.*, Vol. 4, No. 4, 2014.

16. Dong, Y. and G. Wu, "Analysis of short and long term therapeutic effects of radiofrequency hyperthermia combined with conformal radiotherapy in hepatocellular carcinoma," *J. Balkan Union Oncology*, Vol. 21, No. 2, 407–411, Mar. 2016.
17. Nagata, Y., M. Hiraoka, Y. Nishimura, S. Masunaga, M. Mitumori, Y. Okuno, M. Fujishiro, S. Kanamori, N. Horii, K. Akuta, K. Sasai, M. Abe, and Y. Fukuda, "Clinical results of radiofrequency hyperthermia for malignant liver tumors," *Int. J. Radiat. Oncol. Biol. Phys.*, Vol. 38, No. 2, 359–365, May 1997.
18. Shen, L. C. and J. A. Kong, *Applied Electromagnetism*, Ch. 15, CI Engineering, 1995.
19. Li, Y.-L., S. Sun, Q. I. Dai, and W. C. Chew, "Finite element implementation of the generalized-Lorenz gauged $A$-$\Phi$ formulation for low-frequency circuit modeling," *IEEE Trans. Antennas Propagat.*, Vol. 64, No. 10, 4355–4364, Jul. 2016.
20. Zhu, Y. and A. C. Cangellaris, *Multigrid Finite Element Methods for Electromagnetic Field Modeling*, Wiley-IEEE Press, 2006.
21. Barrett, R., M. Berry, T. F. Chan, J. Demmel, J. M. Donato, J. Dongarra, V. Eijkhout, R. Pozo, C. Romine, and H. van der Vorst, *Templates for the Solution of Linear Systems: Building Blocks for Iterative Methods*, SIAM, Philadelphia, 1994.
22. Kim, K., T. Seo, K. Sim, and Y. Kwon, "Magnetic nanoparticle-assisted microwave hyperthermia using an active integrated heat applicator," *IEEE Trans. Microwave Theory Tech.*, Vol. 64, No. 7, 2184–2197, Jul. 2016.
23. Tsuda, N., K. Kuroda, and Y. Suzuki, "An inverse method to optimize heating conditions in RF-capacitive hyperthermia," *IEEE Trans. Biomed. Eng.*, Vol. 43, No. 10, 1029–1037, 1996.
24. Sadiku, M. N. O., *Numerical Techniques in Electromagnetics*, 2nd Edition, Ch. 3, CRC Press, Jul. 2000.
25. Gabriel, S., R. W. Lau, and C. Gabriel, "The dielectric properties of biological tissues: II. Measurements in the frequency range 10 Hz to 20 GHz," *Phys. Med. Biol.*, Vol. 41, No. 11, 2251–2269, Nov. 1996.
26. Wang, H., Y. He, M. Yang, Q.-G. Yan, F.-S. You, F. Fu, T. Wang, X.-Y. Huo, X.-Z. Dong, and X.-T. Shi, "Dielectric properties of human liver from 10 Hz to 100 MHz: Normal liver, hepatocellular carcinoma, hepatic fibrosis and liver hemangioma," *Biomed. Mater. Eng.*, Vol. 24, No. 6, 2725–2732, 2013.
27. Midi, N. S., K. Sasaki, R.-I. Ohyama, and N. Shinyashiki, "Broadband complex dielectric constants of water and sodium chloride aqueous solutions with different DC conductivities," *IEEJ Trans. Electrical Electronic Engineering*, Vol. 9, No. s1, s8–s12, Oct. 2014.
28. Rattanadech, P. and P. Keangin, "Numerical study of heat transfer and blood flow in two-layered porous liver tissue during microwave ablation process using single and double slot antenna," *Int. J. Heat Mass Tran.*, Vol. 58, No. 1–2, 457–470, Mar. 2013.
29. Goumard, C., F. Perdigao, J. Cazejust, S. Zalinski, O. Soubrane, and O. Scatton, "Is computed tomography volumetric assessment of the liver reliable in patients with cirrhosis?," *HPB (Oxford)*, Vol. 16, No. 2, 188–194, Feb. 2014.
30. Astefanoaei, I., I. Dumitru, H. Chiriac, and A. Stancu, "Use of the Fe-Cr-Nb-B systems with low Curie temperature as mediators in magnetic hyperthermia," *IEEE Trans. Magn.*, Vol. 50, No. 11, 7400904, Nov. 2014.
31. Ahmed, M., Z.-J. Liu, S. Humphries, and S. N. Goldberg, "Computer modeling of the combined effects of perfusion, electrical conductivity, and thermal conductivity on tissue heating patterns in radiofrequency tumor ablation," *Int. J. Hyperthermia*, Vol. 24, No. 7, 577–588, Nov. 2008.
32. Ippolito, D., S. Sironi, M. Pozzi, L. Antolini, L. Ratti, C. Alberzoni, E. B. Leone, F. Meloni, M. G. Valsecchi, and F. Fazio, "Hepatocellular carcinoma in cirrhotic liver disease: Functional computed tomography with perfusion imaging in the assessment of tumor vascularization," *Academic Radiology*, Vol. 15, No. 7, 919–927, Jul. 2008.
33. Ippolito, D., C. Capraro, A. Casiraghi, C. Cestari, and S. Sironi, "Quantitative assessment of tumour associated neovascularisation in patients with liver cirrhosis and hepatocellular carcinoma: Role of dynamic-CT perfusion imaging," *Eur. Radiol.*, Vol. 2012, No. 22, 803–811, 2012.

34. Wang, Z., Z. Ying, A. Bosy-Westphal, J. Zhang, B. Schautz, W. Later, S. B. Heymsfield, and M. J. Muller, "Specific metabolic rates of major organs and tissues across adulthood: Evaluation by mechanistic model of resting energy expenditure," *Am. J. Clin. Nutr.*, Vol. 92, No. 6, 1369–1377, Dec. 2010.
35. Urdaneta, M. and P. Wahid, "A study on enhanced hyperthermia treatment for liver cancer using magnetic nanoparticles," *IEEE Microwave RF Conf.*, Dec. 2014.
36. Liu, Z.-J., M. Ahmed, Y. Weinstein, M. Yi, R. L. Mahajan, and S. N. Goldberg, "Characterization of the RF ablation-induced 'oven-effect': The importance of background tissue thermal conductivity on tissue heating," *Int. J. Hyperthermia*, Vol. 22, No. 4, 327–342, Jun. 2006.
37. Lang, J., B. Erdmann, and M. Seebass, "Impact of nonlinear heat transfer on temperature control in regional hyperthermia," *IEEE Trans. Biomed. Eng.*, Vol. 46, No. 9, 1129–1138, Sep. 1999.
38. Nelson, D. A., S. Charbonnel, A. R. Curran, E. A. Marttila, D. Fiala, P. A. Mason, and J. M. Ziriax, "A high-resolution voxel model for predicting local tissue temperatures in humans subjected to warm and hot environments," *J. Biomech. Eng.*, Vol. 131, No. 4, 041003-1–12, Jan. 2009.
39. Rossmann, C. and D. Haemmerich, "Review of temperature dependence of thermal properties, dielectric properties, and perfusion of biological tissues at hyperthermic and ablation temperatures," *Crit. Rev. Biomed. Eng.*, Vol. 42, No. 6, 467–492, Nov.–Dec. 2014.
40. Nieskoski, M. D. and B. S. Trembly, "Comparison of a single optimized coil and a Helmholtz pair for magnetic nanoparticle hyperthermia," *IEEE Trans. Biomed. Eng.*, Vol. 61, No. 6, 1642–1650, Jun. 2014.
41. Pearce, J., A. Giustini, R. Stigliano, and P. J. Hoopes, "Magnetic heating of nanoparticles: The importance of particle clustering to achieve therapeutic temperatures," *J. Nanotechnol. Eng. Med.*, Vol. 4, No. 1, Feb. 2013.
42. Trujillo-Romero, C. J., L. Leija-Salas, and A. Vera-Hernandez, "FEM modeling for performance evaluation of an electromagnetic oncology deep hyperthermia applicator when using monopole, inverted T, and plate antennas," *Progress In Electromagnetics Research*, Vol. 120, 99–120, 2011.